Journal of Turbulence
Vol. 00, No. 00, 2011, 1–26

Large-eddy simulation of turbulent boundary-layer separation from a rounded step

Yacine Bentaleb*, Sylvain Lardeau and Michael A. Leschziner

Aeronautics Department, Imperial College London, Prince Consort Rd, London SW7 2AZ, UK

(*v0.0 submitted July 2011*)

Highly resolved large-eddy simulation is used to investigate the characteristics of a canonical boundary layer separating from a curved step in a channel of height 8.5 times that of the step. The flow is treated as statistically spanwise homogeneous, in line with the conditions of a related experimental study in a large aspect-ratio channel, undertaken within a companion research programme. Primary attention focuses on the details of the separation process and the properties of the separated region, including reattachment. Results are reported and analysed, from a flow-physical perspective, for a wide variety of properties, including wall pressure and skin-friction, mean velocity, Reynolds stresses and related anisotropy maps, two-point-correlation functions, unsteadiness indicators, budgets of the Reynolds stresses and length scales characterising the turbulence and mean-strain fields. The study highlights a range of distinctive features of separation from gently-curved surfaces: the separation process is highly unsteady in time and space; turbulence is highly non-local in character; the mean reverse-flow region is thin and highly elongated; no part of the flow is reversed at all times; the level of production is extremely high following separation, resulting in massive departures from turbulence-energy equilibrium, very high anisotropy and a trend towards one-component turbulence in the separated shear layer. The result, apart from offering insight into the physics of separation, constitute a valuable data set for benchmarking model solutions and investigating statistical turbulence-closure proposals.

Keywords: Large-eddy simulation; Separated shear layer; Anisotropy; Non-equilibrium; Second-moment budgets

1. Introduction

The accurate computational prediction of boundary-layer separation from gently-curved surfaces is at the heart a credible application of CFD to numerous complex engineering flows. Examples are aerodynamic bodies, blades, curved ducts and pipes, cylinders and diffusers. With the exception of transonic flows, in which the wall may be subjected to a strong shock, separation from continuous surfaces is provoked by a relatively gentle adverse pressure gradient decelerating the boundary layer over a significant streamwise distance prior to separation. In most cases, the separating boundary layer is in a turbulent state, notable exceptions being subcritical cylinders, airfoil leading edges and highly-loaded turbomachinery blades—in particular, in the rear-most low-pressure stage of a gas turbine, which usually operates in the low-Reynolds-number regime.

When separation is provoked by a sharp edge—exemplified by the flow past a backward-facing step—the location of the separation is fixed, and the result is a separated shear layer with characteristics similar to an ordinary mixing layer

*Corresponding author. Email: y.bentaleb@imperial.ac.uk

ISSN: 1468-5248 (online only)

DOI: 10.1080/14685240YYxxxxxxx
http://www.informaworld.com

(at least in statistically 2D flow), with weak dependence on the Reynolds number and on the details of the boundary layer. This type of separated flow has been investigated extensively in numerous experimental and computational studies, (see review of Simpson [1] and later work exemplified by [2–9], the last on a swept step).

Separation from a gently curving surface is considerably more complicated than that from a sharp step, because its details depend sensitively on the properties of the boundary layer approaching the separation region. In confined geometries, in particular, there is a pronounced two-way interaction between the outer-flow pressure field acting on the boundary layer and the separation process. In such circumstances, the separation process is highly unsteady, being affected by the turbulent structures within the boundary layer, including the near-wall streaks, and it features intermittently separated and attached patches over a streamwise band around the time-averaged separation line. From a statistical point of view, one recurring observation is that the turbulence-energy and shear-stress levels are extremely high in the vicinity of the nominal separation point and in the initial stretch of the separated shear layer, this being consistent with the highly unsteady nature of the separation process. Another observation is that the separation region is extremely thin, tapering knife-like towards the separation line. This implies the importance of the near-wall processes to the separation behaviour.

In recent years, there have been several simulation studies focusing on separation from curved surfaces. On the one hand, this trend has been encouraged by the rapidly increasing availability, and declining costs, of high-performance computing, allowing highly wall-resolving LES to be performed on separated flows at elevated Reynolds numbers. On the other hand, there has been an increasing realisation that the performance of RANS models in predicting separation from curved surfaces was especially variable—indeed, often very poor—so that high-fidelity DNS and LES for carefully controlled conditions have been deemed essential for assessing alternative RANS models and for identifying the origins of defects of specific closure approximations. Specifically in relation to the last driver, an outstanding advantage of simulations is that these can be exploited, if conducted with great care, to generate benchmark data that are, arguably, more extensive and accurate than experimental data, especially if statistical two-dimensionality is desired. A case in point is the flow in a channel with streamwise-periodic hills on one wall, investigated by Fröhlich et al. [10] and, for a higher Reynolds numbers and finer grids, by Breuer [11]. This geometry has served as a basis for several studies and workshops in which the performance of various RANS and RANS–LES hybrid models have been examined (e.g. [12–14]). An important disadvantage of this geometry is, however, that it is rather unrepresentative of the large majority of real flows. Specifically, the structure of flow approaching separation from any one hill is extremely complex, due to separation, reattachment and acceleration of the flow in the preceding periodic segment. This makes the results derived from RANS models difficult to interpret, because even small modelling errors can translate to large differences in predictive performance as a consequence of periodicity-induced feedback and modelling-error amplification.

Flows that are more amenable to a physical interpretation that has greater general applicability entail the separation of a (close to) canonical turbulent boundary layer and subsequent reattachment and recovery. Computational studies of such flows have been reported by [15–20], the last one being the most elaborate of a number of studies focusing on a boundary layer separating from a 3D hill. Three further studies, by [21–23], deserve to be mentioned, for are all are concerned with separation from a dune-like hump examined experimentally by Greenblatt et

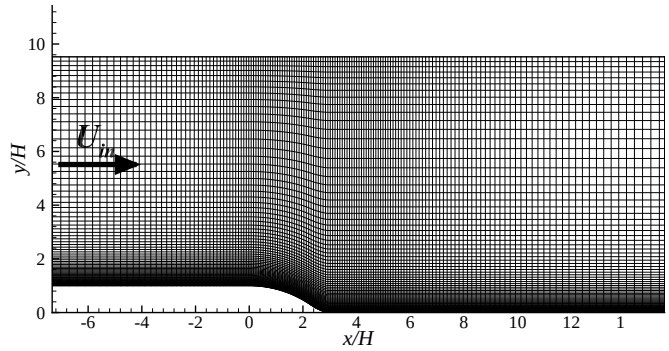

Figure 1. Solution domain and reduced numerical mesh: only every eighth grid line is shown.

al. [24]. In this case, however, separation is almost fixed, because it is provoked by high-curvature contouring in the rear portion of the hump. Several of the above efforts relate to the experimental investigation of Song and Eaton [25] in which an equilibrium boundary layer at $Re = 9100$ was made to separate from a rounded step. While all studies report a range of flow properties and discuss flow-physical features, the scope of the results presented is rather limited, partly because the main emphasis was on assessing approximate modelling schemes [16, 26], or because the simulations were done in the context of flow-control with pulsed jets [15, 18]. In all cases, but the DNS by Dandois et al. [18] and Marquillie et al. [27], grid resolution was relatively modest, in the range 1.5–7 million nodes. This prevented results beyond second moments and flow-structure information being extracted at acceptable accuracy.

This paper presents the outcome of highly-resolved LES simulations, with meshes containing up to 24 million nodes, for a rounded step that is a variation of the step used by Song and Eaton [25]. Specifically, the step geometry was modified to create a larger and more vigorous separation zone, resulting in a higher step-height Reynolds number with virtually the same momentum-thickness Reynolds number of the upstream boundary layer. The simulations formed part of a broader study on the control of separation with circular synthetic jets, documented in Lardeau and Leschziner paper [28]. Exceptionally, within the group of studies on the same theme, this paper reports and analyses second-moment budgets, in addition to a wide range of other statistical and structural properties. Agreement between selected results of the LES and available experimental data of Zhang and Zhong [29] has been discussed in [28], and this discussion is not repeated herein. Rather, this paper confines itself to a comprehensive analysis of the LES data.

2. Flow configuration

The geometry under consideration is shown in figure 1. The rounded ramp of height H is placed in a high-aspect-ratio duct with upstream height of $8.52H$. In the simulations, the flow is assumed to be spanwise homogeneous, with the spanwise slab being $3.17H$. The assumption of homogeneity is justified by the fact that the experimental ratio of duct depth to the step height was 38. In the experiment, tripped boundary layers were allowed to develop on both walls for a distance of about $25H$. The Reynolds number, based on H and the inlet free-stream velocity $U_{\rm in}$, is 13700. At $x/H = -7.34$, the computational inlet, the momentum-thickness Reynolds number is $Re_\theta = 1190$, and the boundary-layer thickness is $\delta_{99} = 0.80H$.

Table 1. Grid resolution and respective separation and reattachment positions.

Computation	Grid	$(x/H)_s$	$(x/H)_r$
RUN 1	$448 \times 128 \times 192$	0.87	4.21
RUN 2	$768 \times 160 \times 192$	0.83	4.36

LDA measurements at this location have shown the boundary layers to be very close to the canonical equilibrium state. The manner in which the inlet conditions were specified in the simulation is explained in the following section.

The step geometry is based on that used originally by Song and Eaton [25]. Thus, the height of the step was increased by a factor of 1.5 in order to enlarge the separation bubble, which was regarded as being rather weak in [25]'s experiment. This adaptation was undertaken interactively with a parallel experimental effort by Zhang and Zhong [29]. The step shape is described by the following three relations, with the origin $x/H = 0$ being the upstream edge of the ramp:

$$\begin{aligned} y_{\text{wall}} &= (1 - R_1) + \sqrt{R_1^2 - x^2} \qquad \text{for} \qquad 0 < x/H < 2.3 \\ y_{\text{wall}} &= y_2 - \sqrt{\tfrac{R_1^2}{4} - (x_2 - x)^2} \qquad \text{for} \qquad 2.3 < x/H < 2.835 \\ y_{\text{wall}} &= R_2 - \sqrt{R_2^2 - (3 - x)^2} \qquad \text{for} \qquad 2.835 < x/H < 2.937 \end{aligned} \tag{1}$$

with $R_1 = 4.03$, $R_2 = 0.333$, $x_2 = 3.449$ and $y_2 = 1.936$. The distance from the bottom wall $y_w = (y - y_{\text{wall}})$ is also used throughout the text.

3. The computational approach

Implicitly filtered LES momentum and continuity equations for incompressible flow were solved over a general non-orthogonal, boundary-fitted, multi-block finite-volume mesh. The solution is based on a fractional-step time-marching method, with the time derivative approximated by a third-order Gear scheme [30]. The fluxes are approximated by second-order centred approximations. Within the fractional-step algorithm, a provisional velocity field results from advancing the solution with the flux operators. This is then corrected through the pressure field by projecting the provisional solution onto a divergence-free velocity field. To this end, the pressure is computed as a solution to the pressure-Poisson problem with the aid of a V-cycle multigrid scheme. In order to suppress unphysical oscillations, associated with pressure-velocity decoupling, a practice equivalent to that introduced by Rhie and Chow [31] is adopted. Fishpool and Leschziner [30] demonstrate that the loss of accuracy associated with the smoothing introduced by this practice is minimal.

Simulations were performed with two grids having 11 million (RUN 1) and 24 million nodes (RUN 2), respectively (table 1). Most results included herein were derived from the latter simulation, unless grid-dependence is illustrated. The differences between the two sets of results are very modest in most respects. For the lower wall, the streamwise variations of the cell dimensions, normalised by the local friction velocity, are shown in figure 2. While scaling with the friction velocity may be argued to be inappropriate in the separated region, the sole purpose of the distributions in figure 2 is to support statements on the resolution of the near-wall region. An alternative scaling is that of [32], which combines the friction velocity

with a velocity scale derived from the streamwise pressure gradient. This blended scaling was found to result in distributions very similar to those shown in figure 2, except in the immediate vicinity of the stagnation points, where scaling with u_τ obviously results in zero values. The distance of the wall-nearest cell centre to the wall is $\Delta y^+/2 < 1$. Within the range $x/H = 0$–5.0, the spanwise cell dimension, Δz^+, is 5–13, while the streamwise cell dimension, Δx^+, is below 12 (figure 2). The boundary layer on the upper wall was covered by a coarser grid than that on the lower wall, with the conditions between the wall and the wall-nearest y^+ location of around 25 being covered by a log-law wall function, and with about 10 grid nodes covering the boundary-layer thickness. This choice is justified by the fact that the upper boundary layer is far away from the region of interest, is only subjected to a weak adverse gradient and is always fully attached. An entirely analogous approach was taken by Fröhlich et al. [10] when simulating the flow at a similar Reynolds number in a much tighter channel with massive separation behind streamwise periodic hill-shaped obstructions on the lower wall. In that case, this choice was made after extensive grid-sensitivity trials, and it is now well established that the resulting solution, including budgets, is fully trustworthy.

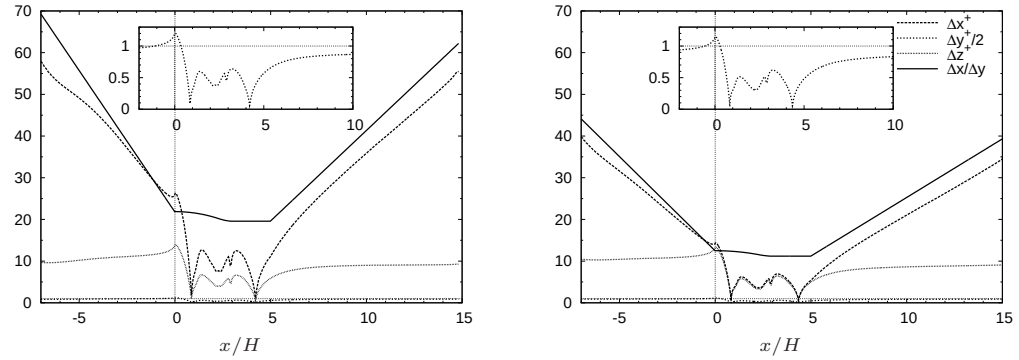

(a) RUN 1 (b) RUN 2

Figure 2. Grid spacings in wall units and aspect ratio $\Delta x/\Delta y$ along the bottom wall. The inserts in the figures show a magnified view of the normal grid spacing $\Delta y^+/2$.

Turbulent boundary layers were imposed at the domain inlet ($x/H = -7.34$) on both the upper and lower walls. To this end, data were taken from a precursor simulation, performed with the aid of a recycling method [33], for a stretch of a boundary layer developing in the actual channel. At a streamwise position at which $Re_\theta = 1190$, every realisation of the velocity field was stored over a period of $1120H/U_{\rm in}$. This data set was then used to explicitly prescribe the inlet condition. Comparisons between lower-wall boundary-layer data returned by the present precursor simulation and DNS results of Jimenez et al. [34], for a similar Reynolds number, $Re_\theta = 1100$, are shown on figure 3; agreement is seen to be close. As a result, a high-fidelity representation of the boundary layer approaching the step is obtained. This is shown in figure 4, which compares present results for the turbulence energy, Reynolds stresses and the budget for the streamwise and spanwise Reynolds stresses at the streamwise station $x/H = -4.0$ with DNS data of Jimenez et al. [34].

The quality of the resolution is conveyed in figure 5 by way of three indicators: the ratio of maximum cell dimension to the Kolmogorov scale, the latter obtained from the dissipation rate as part of the turbulence-energy budget; the ratio of the RANS-equivalent turbulent viscosity and the fluid viscosity, the former obtained from k^2/ε; and the ratio of subgrid-scale viscosity to fluid viscosity, obtained with the mixed-time-scale model of Inagaki et al. [35]. Thus, within the recirculation

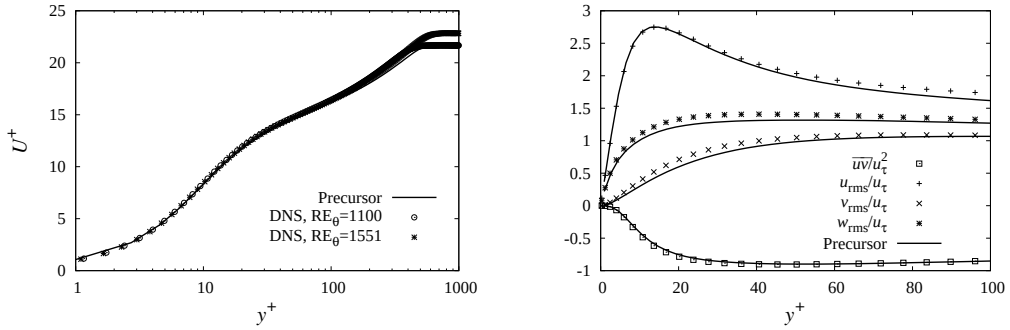

(a) Mean streamwise velocity.

(b) Mean Reynolds stresses.

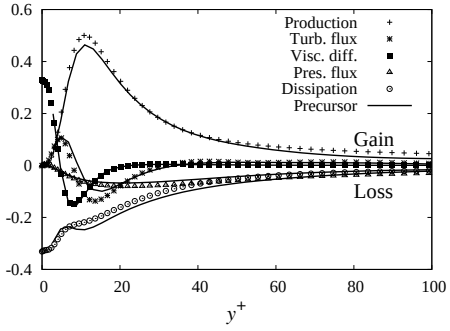

(c) Budgets of $\overline{uu}$.

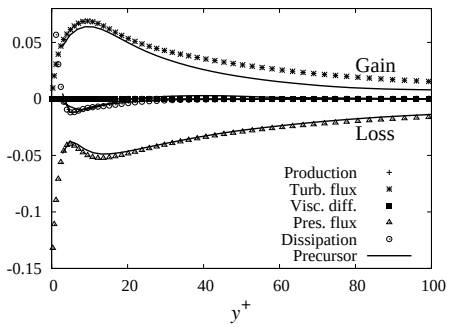

(d) Budgets of $\overline{ww}$.

Figure 3. Comparison of inflow conditions with DNS data of a turbulent boundary-layer flow [34]. Lines: LES data from precursor simulation (profiles are normalized by the friction velocity); symbols: DNS data at $Re_\theta = 1100$.

zone, the maximum cell dimensions are around 6–9 Kolmogorov lengths, while the ratio of turbulent viscosity to the fluid viscosity is of order $1\text{–}2 \times 10^3$. Consistently, the subgrid-scale viscosity is low—below 0.24 of the fluid viscosity. Finally, the resolved dissipation was observed to be of order 70% of the level determined from balancing all the other terms in the turbulence-energy budgets, to be discussed later.

The time step corresponds to a maximum cell-CFL value of around 0.5. Simulations were run for 300 time units, one time unit being H/U_{in}, before statistical sampling commenced. The flow was then computed for further 1700 time units during which data for various statistical properties were gathered. Statistical convergence was increased by spanwise averaging.

4. Results

4.1. *Overall view and major characteristics*

Two instantaneous realisations of the flow are given in figures 6 and 7, by way of velocity contours and iso-surfaces of the Q-criterion, respectively. In the latter, colours indicate variations in streamwise velocity—red denoting high values, yellow and green moderate values and blue low values. The former realisation, and others like it, demonstrate that instantaneous, local separation extends over a substantial distance across the surface of the rounded step. The time-averaged separation location is at $x/H = 0.83$, but the PDF of the upstream-most local separation point (included in Lardeau and Leschziner [28] paper) indicates that

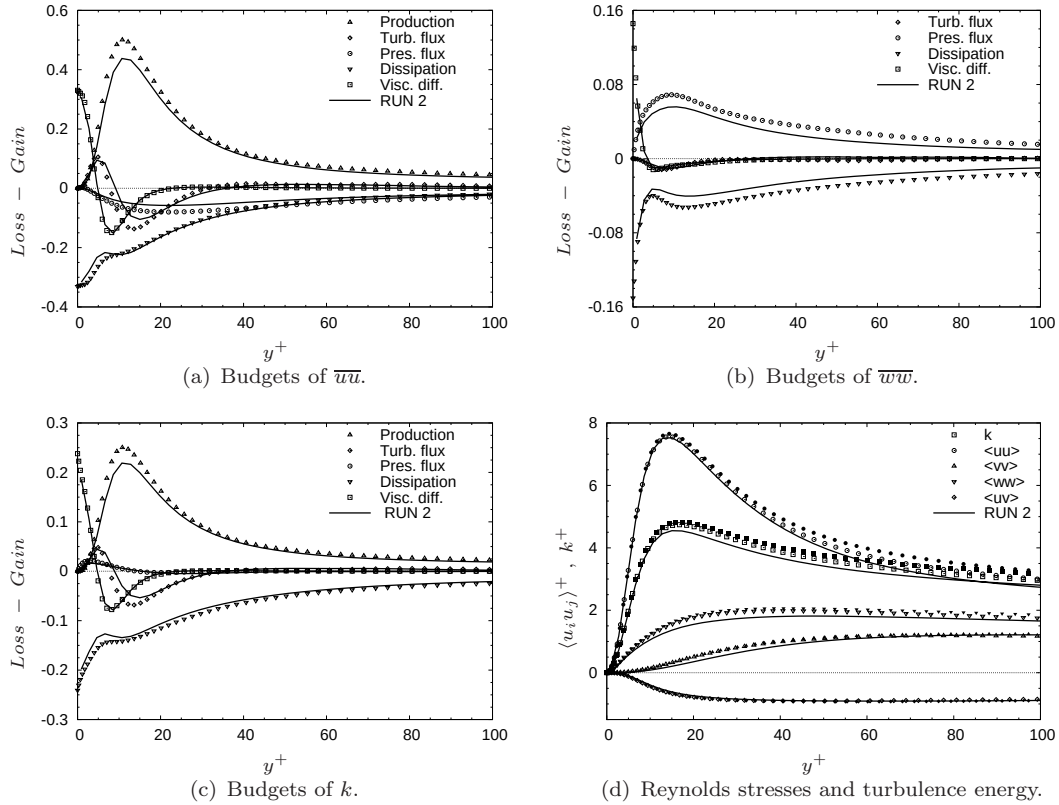

(a) Budgets of $\overline{uu}$. (b) Budgets of $\overline{ww}$.

(c) Budgets of k. (d) Reynolds stresses and turbulence energy.

Figure 4. Comparison of LES simulation with DNS data of a turbulent boundary layer flow [34] at $x/H = -4.0$, where $Re_\theta \sim 1060$. Lines: LES data, profiles are normalized by the friction velocity; open symbols: DNS data at $Re_\theta = 1100$; closed symbols: DNS data at $Re_\theta = 1551$.

the instantaneous separation extends from around $x/H = 0.6$ to 1.5. Given that the spanwise slab, shown in figure 6, extends over $L_z^+ = 2000$, visual inspection of the separation pattern suggest structures that are of order 100 wall units apart, a distance that is resolved by around 9–10 spanwise cells and one that is in agreement with other results for inter-streak separation in channel flow and boundary layers (e.g. [36]). This inter-streak distance is confirmed in figure 8, which shows the streamwise variation of the spanwise correlation function R_{uu} at two distances from the wall, corresponding to $y^+ = 15$ and $y^+ = 100$ at $x/H = 0$. In particular, the distribution at $x/H = 0$ reveals a minimum at around $z^+ = 80$, corresponding to one-half the inter-streak (low-speed-to-low-speed or high-speed-to-high-speed) distance. Further downstream, following separation, the turbulence structures grow rapidly, and the correlation function follows suit, maintaining a value of 0.2 at dz^+ of approximately 400. As this value is only one-fifth of the extent of the spanwise box, the implication is that this box is sufficiently wide to capture all important structures in the simulation. The Q-criterion plotted in figure 7 gives qualitative support for the above observations. Thus, spanwise-elongated structures are observed in the upper portion of the separated shear layer with a typical length of around one-quarter to one-third of the spanwise box. These structures may be associated with the Kelvin–Helmholtz (KH) instability in the shear layer. In Lardeau and Leschziner's [28] study, it is shown, based on energy spectra derived from the coarser-grid simulation, that the energy peaks at the Strouhal number $St_H = fH/U_{\text{in}} = 0.2$, corresponding to the so-called "flapping instability". Moreover, the spectrum features another weak peak at a frequency that corresponds to the first sub-harmonic of the KH mode.

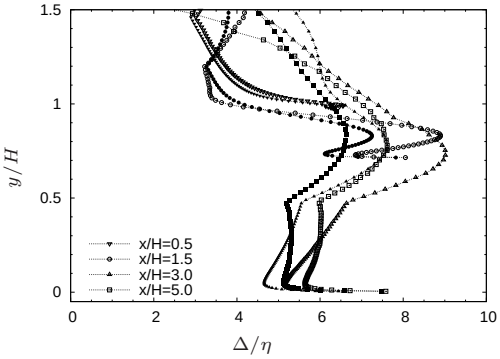

(a) Ratio of maximum cell dimension to the Kolmogorov length scale.

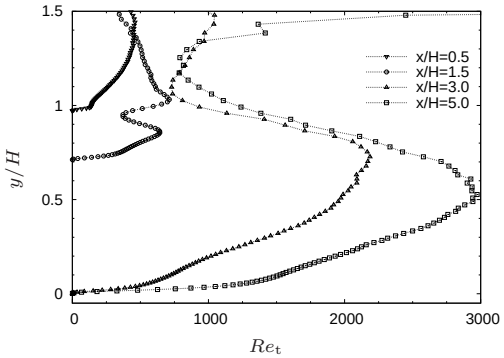

(b) Turbulent Reynolds number $Re_t = k^2/\nu\varepsilon$.

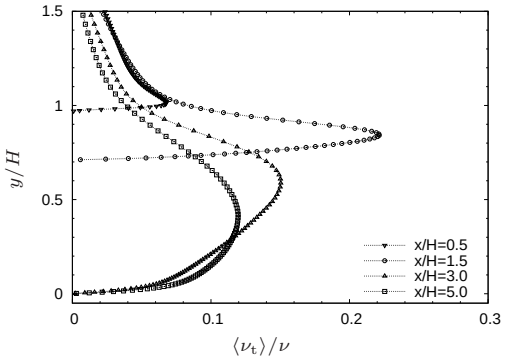

(c) Normalised subgrid-scale viscosity.

Figure 5. Assessment of the resolution—In the Kolmogorov length scale $\eta \equiv (\nu^3/\varepsilon)^{1/4}$ (figure 5(a)), the dissipation rate ε is either determined from balancing all the other terms in the k-budget (open symbols) or evaluated explicitly (closed symbols)).

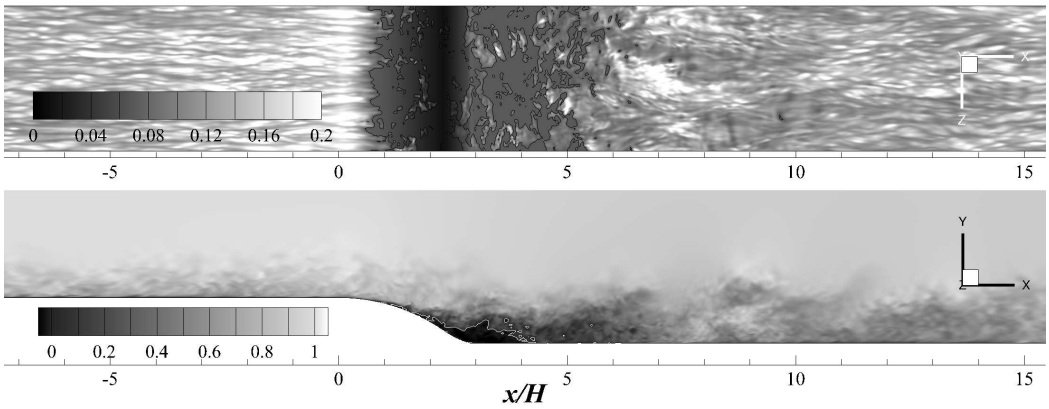

Figure 6. Instantaneous streamwise velocity. Top view at a distance $y^+ = 15$ (with u_τ at $x/H = 0$) from the surface, corresponding to the surface $y/H \sim 0.02$; side view at spanwise mid-plane. Gray regions bordered by lines indicate reversed flow.

Figure 6, as well as animations, show that patches of attached flow exist along the entire region downstream of the mean separation point. A statistical representation of this fact is conveyed in figure 9. This figure shows contours, in the spanwise plane, of the proportion of time the flow is reversed—essentially the probability of reverse flow. The thick dashed line represents the zero time-averaged streamwise velocity locus, *i.e.* the line signifying the height of the time-mean reverse-flow layer, and this matches with the contour 0.5. As seen, there is only a small patch within which the flow is reversed for 90% of the time, and there is no region in which the flow is reversed at all times. The locus 0.1 intersects $y_w/H = 0$ at $x/H = 0.7$,

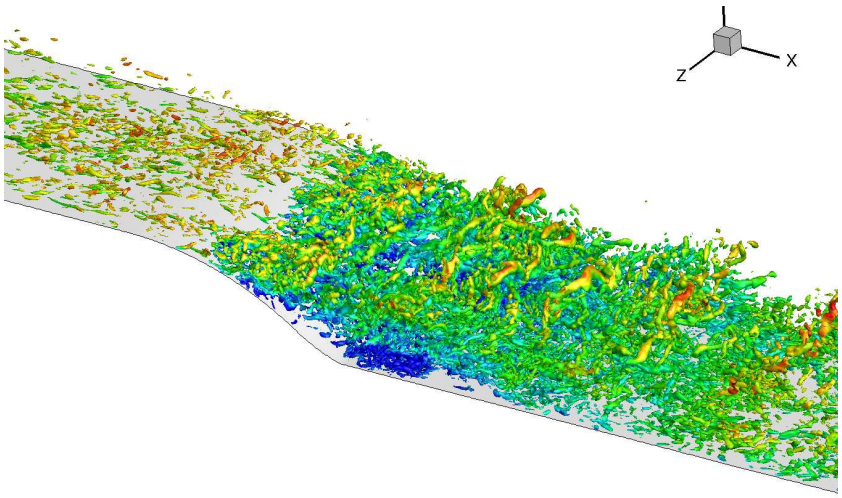

Figure 7. Isosurface of the Q-criteria ($Q = 5U_{\text{in}}^2/H^2$), colored by the streamwise velocity.

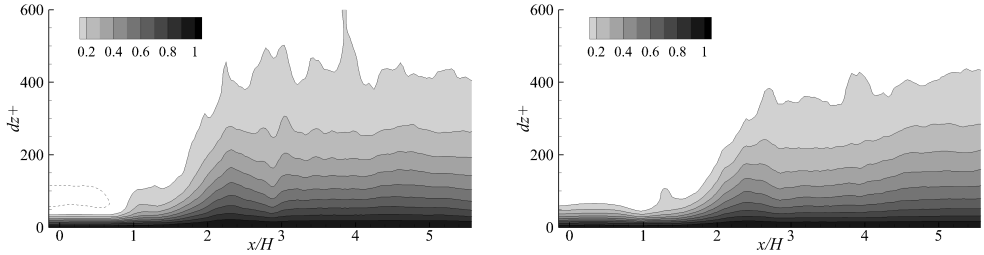

Figure 8. Spanwise two-point velocity correlation for two different distances from the surface ($y^+ = 15$ and $y^+ = 100$ at $x/H = 0$) along the streamwise direction.

confirming a statement made earlier about the PDF of the upstream-most location of separation being at around $x/H = 0.6$.)

Figure 10 shows contours of two sets of two-point correlation functions, in the spanwise plane, one for streamwise-velocity fluctuations, R_{uu}, and the other for pressure fluctuations, R_{pp}, at four positions in the flow. The shaded contours relate to the former, while the lines identify the latter. The contours for R_{uu} are fairly narrowly confined in the wall-normal direction, especially those indicating high correlation levels, but elongated in the streamwise direction, primarily with a forward orientation. The growth of the correlation domain, both in the streamwise and lateral directions, is consistent with the increased size of turbulence structures with downstream distance as separation is approached and beyond separation. A useful qualitative message that R_{uu} conveys is that the degree of non-locality of turbulence is generally high and increases substantially following separation. In fact, close to the position of reattachment, the correlation region is extensive, being of the same order as the whole recirculation region. This issue of non-locality is especially important in relation to the validity of single-point-closure principles. The contours of R_{pp} differ greatly from those pertaining to the velocity fluctuations. The main point of distinction is the large wall-normal extent of the correlation domain and the much higher level of correlation value over large distances. This is, qualitatively, consistent with the elliptic nature of the pressure-fluctuation field, and more specifically, with the role of wall-reflection processes, which cause pressure fluctuations to propagate across the flow and result in pronounced wall-normal coherence in the correlation function. Here again, the message is that non-locality is very high, and that the formulation of single-point approximations to the statistical

terms representing pressure-velocity interactions is based on a weak foundation.

The characteristics described above convey a complex, highly unsteady separation process that points to a tenuous balance between the diffusive processes that favour attachment and the gradually increasing adverse-pressure gradient that tends to provoke and maintain separation. Reattachment is even more patchy than separation (figures 6 and 9), with the reattachment location extending, instantaneously, over most of the separated zone, down to around $x/H = 5.5$, relative to a time-averaged reattachment at $x/H = 4.36$, determined from the wall-shear stress.

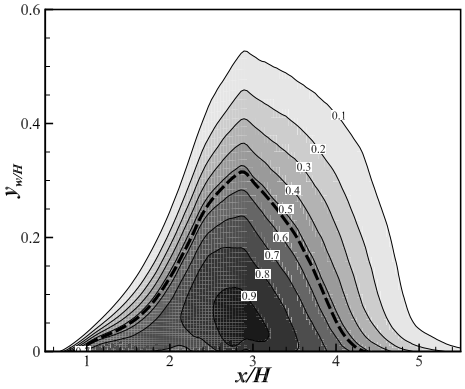

Figure 9. Contours of the probability of reverse streamwise velocity. The dashed line represents the zero time-averaged streamwise velocity locus.

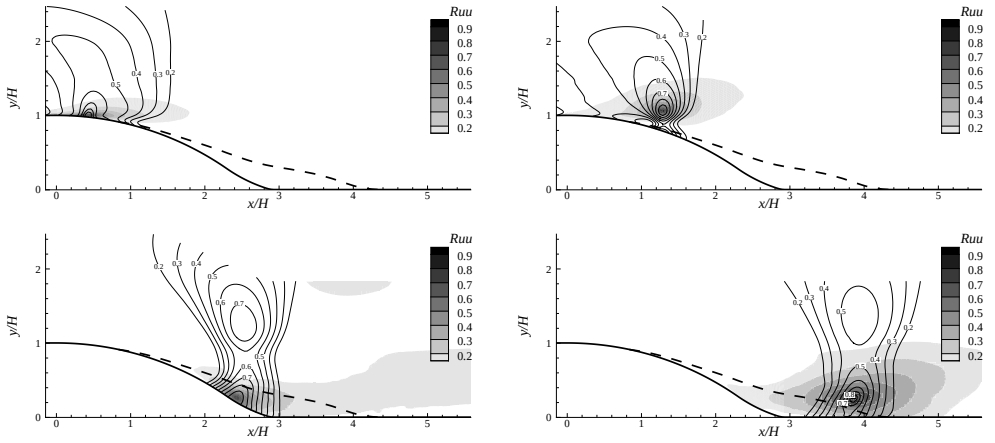

Figure 10. Contours, in the spanwise plane, of two points correlations R_{uu} (color scale) and R_{pp} (lines) at four different points.

The time-averaged stream-function field is shown in figures 11 and 12. The latter includes magnified views of the separation and reattachment regions to bring out more clearly the very shallow angle of the zero-streamline, especially at the separation end. Also included is the zero-streamwise-velocity locus, essentially bisecting the recirculation zone. The separated region is seen to be extremely thin and elongated following separation. As will be shown later, this region is marked, despite its close proximity to the wall, by a rapid increase in turbulence energy and shear stress, due to very high production. In fact, the highest production occurs at around $x/H = 1.4$, which is close to the separation point, $x/H = 0.83$, thus indicating a high level of fluctuations implied by the pattern in figure 6. The reattachment angle is around 10°, and this particular parameter is a sensitive indicator of the delicate near-wall balance between a gain and loss contributions in

the shear-stress budget. RANS models, especially those based on second-moment closure, have great difficulties representing this region realistically.

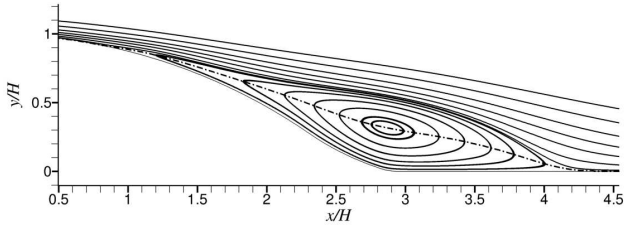

Figure 11. Streamline contours of the time-averaged flow field in the recirculation region. The dashed-dot line represents the zero-streamwise-velocity locus.

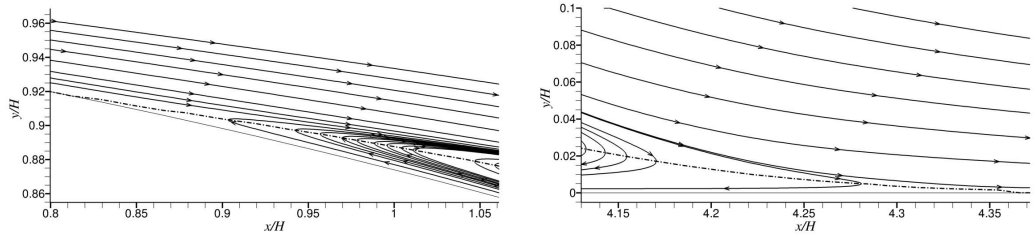

(a) Separation: $x/H = 0.83$. (b) Reattachment: $x/H = 4.36$.

Figure 12. Streamline contours of the time-averaged flow field: magnified views of the separation and reattachment regions.

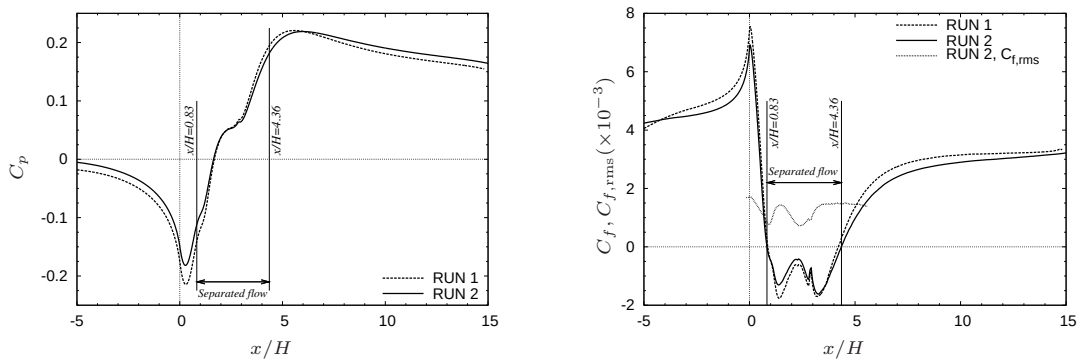

(a) Pressure coefficient. (b) Skin-friction coefficient.

Figure 13. Distribution of pressure and skin-friction coefficients along the lower wall.

Streamwise distributions for the pressure and skin-friction coefficients are shown in figure 13. In this particular figure, solutions obtained with 11 million (RUN 1) and 24 million nodes (RUN 2) are compared. Both coefficients indicate that the near-wall layer accelerates well upstream of the step, due to distortions in the velocity field in the downstream curved section associated with the attached near-wall flow maintaining a near-constant vorticity as it curves downwards. As the flow progresses downstream, just beyond $x/H = 0$, the overall deceleration causes a pressure rise on the surface and the near-wall flow decelerates until separation occurs at $x/H = 0.83$. The unevenness in the skin-friction coefficient within the separated region is due entirely to curvature discontinuities in the surface shape, and very similar distributions arise with both grids. The pressure coefficient features a weak plateau with centre around $x/H = 2.7$, this weakness reflecting the thin and elongated shape of the separation bubble—in particular the thin separation and reattachment tongues at either end of the bubble. The surface pressure

reaches a maximum close to the reattachment point, and the flow is seen to recover towards an equilibrium channel condition beyond $x/H = 10$. Figure 13(b) also contains the streamwise variations of the r.m.s. of the skin-friction coefficient, which is appropriately viewed in conjunction with figure 9. The r.m.s. level is of the same order as the mean skin friction itself, and this signifies the substantial unsteadiness that prevails in the separated region. As the probability of near-wall reverse flow in the region $1 < x/H < 4$ is of order 0.7, the near-wall flow is intermittently attached and separated, leading to very high r.m.s. values, relative to the mean, in the near-wall velocity and hence in the skin friction.

4.2. *Velocity and Reynolds-stress profiles*

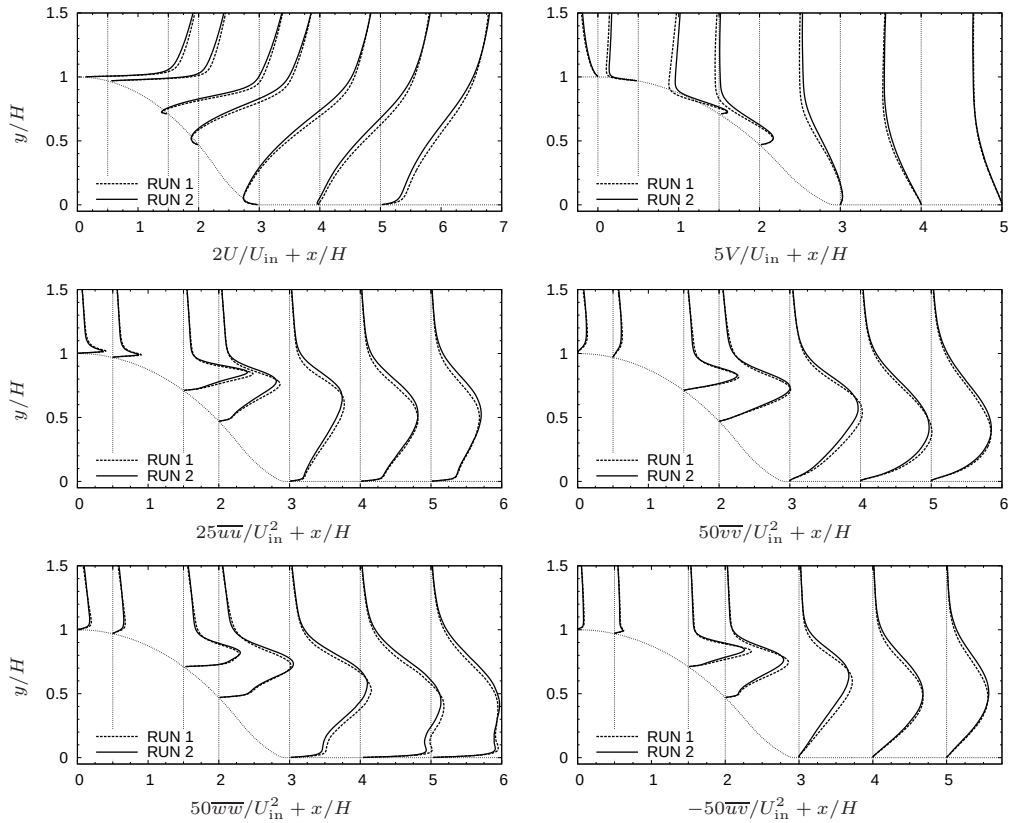

Figure 14. Mean velocity and Reynolds stress profiles at various vertical locations: $x/H = 0$, 0.5, 1.5, 2, 3, 4, and 5. Note that scaling multipliers are used to simply gain an equally clear view of the variations for all quantities.

Six sets of 7 profiles, for velocity, Reynolds stresses and turbulence energy, respectively, are given in figure 14. The locations have been chosen to provide a representative view of the three major flow regions: the attached boundary layer ($x/H = 0$ and 0.5), the recirculation zone ($x/H = 1.5$, 2, 3 and 4) and the post-reattachment flow ($x/H = 5$).

The velocity profiles are akin to those observed in most separated flows, except in so far as that they accentuate the fact that the reverse-flow region here is very thin, especially following separation and preceding reattachment, reaching a maximum of only $0.33H$ at $x/H = 2.9$, and that the maximum reverse-flow velocity is low, at only 13%, reached at $x/H = 3.0$. The last U-profile is in the post-reattachment region, and its shape indicates the acceleration of the near-wall layer associated

with the preceding impingement, coupled with the formation of the new boundary layer in this region.

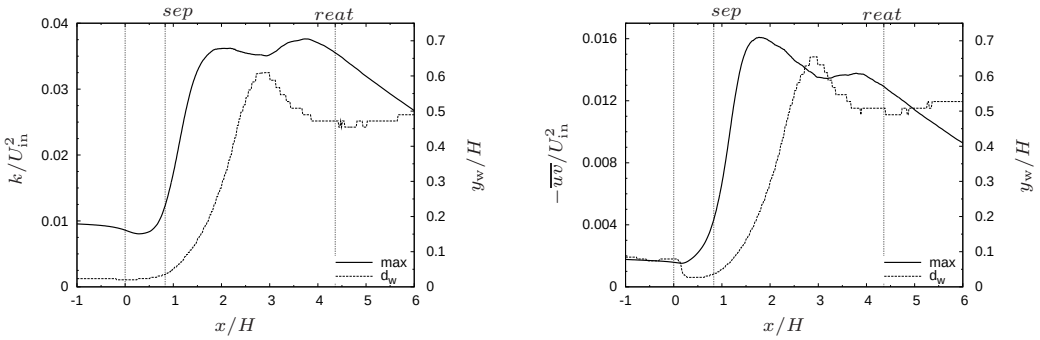

Figure 15. Streamwise evolution of the maximum turbulence energy and shear stress (solide lines). The vertical distance to the bottom wall, d_w, of these maxima is included (dashed lines).

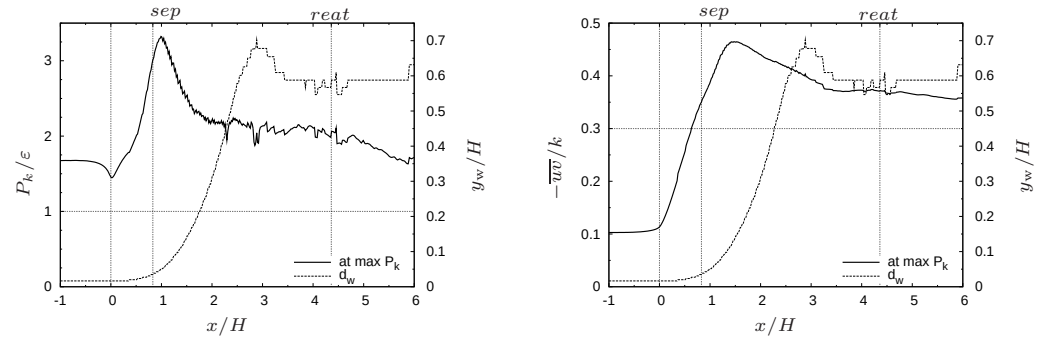

Figure 16. Streamwise evolution of the ratios P_k/ε and $-\overline{uv}/k$ at $P_{k_{max}}$ y-locus (solide lines). The vertical distance to the bottom wall of the $P_{k_{max}}$ y-locus is included (dashed lines).

The profiles of the Reynolds stresses reveal a steep rise in turbulence activity following separation. This rise is brought out particularly well in figure 15, which shows the streamwise variations of the maximum turbulence energy, k, and the shear stress, $-\overline{uv}$, their respective vertical distance to the bottom wall being identified by the dashed lines and denoted by d_w. Both quantities start rising upstream of the separation point and reach a maximum at around $x/H = 1.8$, *i.e.* $1.0H$ downstream of the mean separation point. In addition, k and $-\overline{uv}$ feature two maxima, separated by a weak dip that is associated with the upward turning of the flow where the curved step merges into the horizontal wall.

The features described above suggest that the separated shear layer is far from turbulence-energy equilibrium. This is confirmed by figure 16, which shows the ratio of turbulence production to dissipation, P_k/ε, and the ratio of $-\overline{uv}/k$, both along the locus of maximum turbulence-energy production. The former ratio is seen to reach about 3.3 immediately downstream of the separation point, not dropping below 2 until reattachment. Consistently, $-\overline{uv}/k$ is significantly above 0.3, reaching a maximum value of 0.46, again close to the separation point. Attention is drawn to the fact that both ratios need to be viewed with caution upstream of separation, because of the particular choice of loci along which the ratios were determined.

Figure 14 shows that the transverse stresses, $\overline{vv}$ and $\overline{ww}$, are close to each other over a substantial portion of the separated layer, reflecting the near-symmetric redistribution of energy from dominant streamwise, $\overline{uu}$, to the transverse stresses. A clearer, quantitative, view of the variation of the anisotropy will be conveyed below by reference to anisotropy invariants. Before this is done, however, it is noted, upon inspection of figure 14, that the bulging of the $\overline{uu}$ and $\overline{ww}$ profiles, in

contrast to the $\overline{vv}$ profile, is a first indication of the trend towards two-component turbulence very close to the wall, demonstrated quantitatively later. The bulging in the $\overline{ww}$ is especially remarkable, and is an indicator, again explored later, of a strong, preferential transfer of energy from $\overline{uu}$ to $\overline{ww}$ due to "splatting", *i.e.* pressure-velocity interaction. The shear stress is observed to grow dramatically after separation, and this is the reason for the very gradual growth of the separated region: the flow resists separation despite the strong adverse pressure gradient by virtue of the steep increase in mixing. An analogous behaviour was observed in separation from a 3D hill, based on simulations by Garcia-Villalba et al. [20]. The above behaviour of turbulence around the separation point is among the most challenging to represent statistically, and is also one of the most potent sources of error in RANS modelling of separation from curved surfaces.

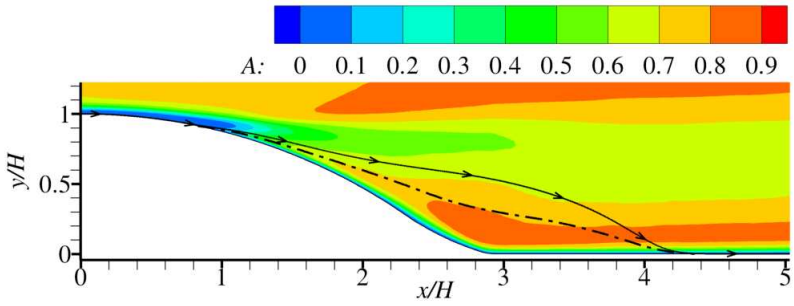

(a) Flatness parameter A.

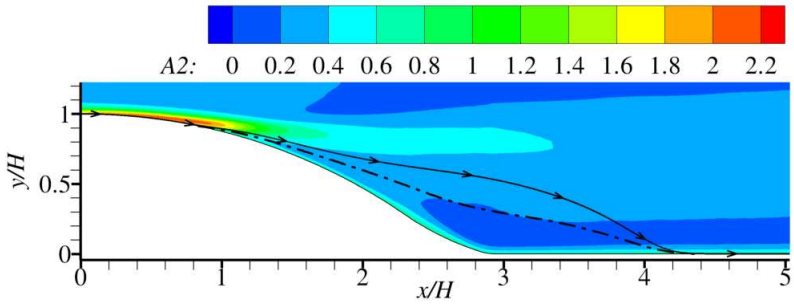

(b) Second invariant A_2.

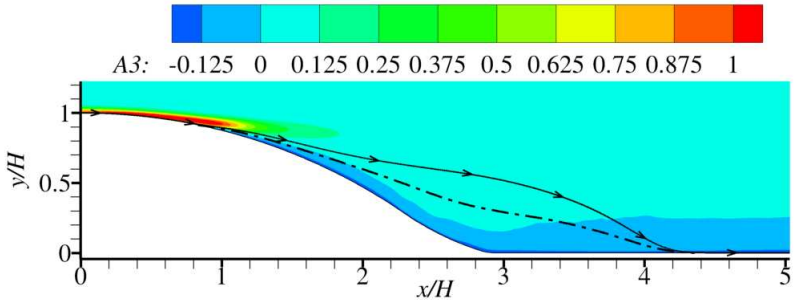

(c) Third invariant A_3.

Figure 17. Contours of stress anisotropy parameters (equation (2)). The dashed-dot line represents the zero-streamwise-velocity locus.

Anisotropy properties are presented in figures 17–19 in three ways: figure 17 gives a global view of the flatness parameter as well as the second and third anisotropy

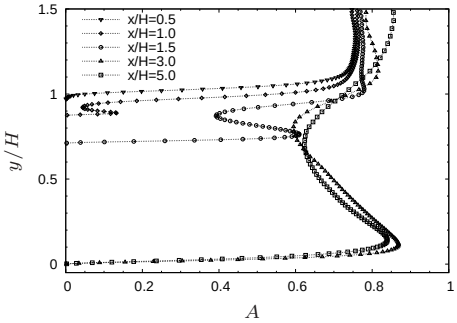

(a) Flatness parameter A.

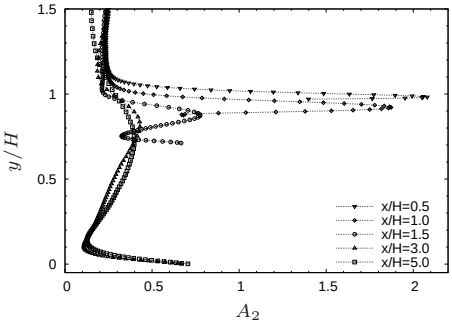

(b) Second invariant A_2.

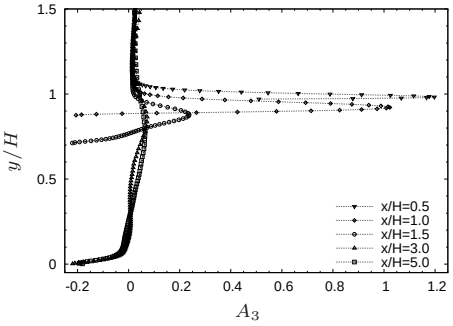

(c) Third invariant A_3.

Figure 18. Profiles of stress anisotropy parameters (equation (2)) at selected streamwise locations.

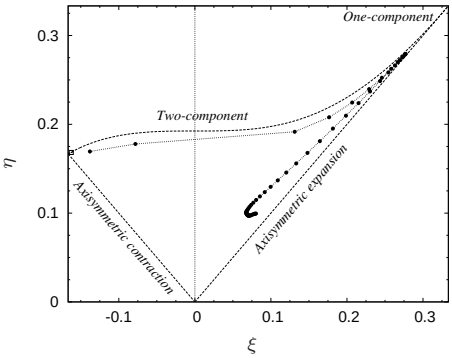

(a) $x/H = 1.0$.

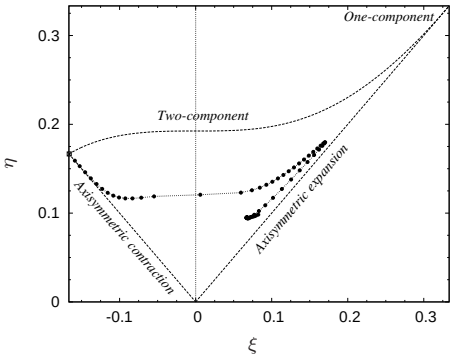

(b) $x/H = 1.5$.

Figure 19. Anisotropy-invariant mapping at two streamwise locations, with $y/H \leq 1.5$. The open square symbol stands for the nearest point to the bottom wall.

invariants, respectively:

$$A = 1 - \frac{9}{8}(A_2 - A_3), \qquad A_2 = a_{ij}a_{ji}, \qquad A_3 = a_{ij}a_{jk}a_{ki}, \tag{2}$$

where

$$a_{ij} = \frac{\overline{u_i u_j}}{k} - \frac{2}{3}\delta_{ij};$$

figure 18 shows profiles of these same invariants at selected streamwise locations; while figure 19 shows, for the positions $x/H = 1.0$ and 1.5, the relationship between the parameters η and ξ, representing, respectively, the second and third invariants, A_2 and A_3, via:

$$6\,\eta^2 = A_2/4; \qquad \text{and} \qquad 6\,\xi^3 = A_3/8, \tag{3}$$

along cross-flow traverses, in the range $y/H < 1.5$, within the "Lumley triangle". The two streamwise stations chosen relate, respectively, to the immediate post-separation zone and the position at which the turbulence energy and the shear stress are close to their respective maxima following separation.

With attention focusing first on the separated shear layer, it is observed, especially in figure 18, that the flatness parameter drops to low minima (of order 0.1) in the early stages of separation (around $x/H = 1.0$), driven primarily by high values of A_2 (of order 2), but counteracted by somewhat lower values of A_3 (of order 1). This behaviour is associated with the strong rise, by production, in streamwise fluctuations, matched only gradually by the redistribution process as the shear layer evolves and diverges from the wall. In the Lumley triangles, figure 19, the central portion of the shear layer is identified by the right-hand-side sharp peak. Thus, the turbulence state has features akin to one-component turbulence, in which one eigenvalue of the stress tensor dominates, consistent with a highly-elongated, *cigar*-like shape of the deviatoric Reynolds-stress tensor. Further downstream, including in the recovering wake, anisotropy weakens, as shear-generation declines and redistribution operates more effectively, but is still substantial in central portions of the shear layer (of order 0.6), with A_3 close to zero and A_2 of order 0.4. Hence, over a major proportion of the flow, A is essentially dictated by A_2. In the outer portion of the shear layer, turbulence is in a state not far from isotropy ($A = 0.8$), associated with low strain-induced production and effective redistribution.

Figure 19 shows, first, that the turbulence field approaches a two-component state very close to the wall. As is also evident from figure 18, this region is characterised by steeply rising A_2 and negative values of A_3. This behaviour implies a *pancake*-like shape of the deviatoric Reynolds-stress tensor, with broadly equal eigenvalues associated with wall-parallel fluctuation components and rapidly diminishing wall-normal component. Within the reverse-flow portion of the recirculation region, away from the immediate vicinity of the wall, where the reverse-flow layer reaches its minimum velocity, straining is weak, turbulence intensity is high, and the turbulence tends to move away from the state of two-component turbulence towards the isotropic state. In the Lumley triangle pertaining to $x/H = 1.5$, this region corresponds to the plateau of the cross-flow locus, and the beginning of this trend is discernible already at $x/H = 1.0$ at which the reverse-flow layer is still extremely thin.

4.3. *Budgets*

A few aspects of the budgets, associated with turbulence production and dissipation, have already been highlighted in the previous section. Here the budgets are discussed in detail.

With the pressure-velocity interaction terms decomposed into pressure-strain and pressure-diffusion fragments, the budgets may be written as follows:

$$\frac{D\overline{u_i u_j}}{Dt} = P_{ij} - \varepsilon_{ij} + T_{ij} + \Phi_{ij} + D_{ij} + V_{ij}; \tag{4}$$

$$P_{ij} = -\overline{u_j u_k}\frac{\partial U_i}{\partial x_k} - \overline{u_i u_k}\frac{\partial U_j}{\partial x_k}; \qquad \varepsilon_{ij} = 2\nu\overline{\frac{\partial u_i}{\partial x_k}\frac{\partial u_j}{\partial x_k}}; \qquad T_{ij} = -\frac{\partial \overline{u_i u_j u_k}}{\partial x_k};$$

$$\Phi_{ij} = \overline{\frac{p}{\rho}\left(\frac{\partial u_i}{\partial x_j} + \frac{\partial u_j}{\partial x_i}\right)}; \qquad D_{ij} = -\frac{1}{\rho}\left(\frac{\overline{pu_j}}{\partial x_i} + \frac{\overline{pu_i}}{\partial x_j}\right); \qquad V_{ij} = \nu\frac{\partial^2 \overline{u_i u_j}}{\partial x_k \partial x_k};$$

where P_{ij}, ε_{ij}, T_{ij}, Φ_{ij}, D_{ij} and V_{ij} represent, respectively, production, dissipation, turbulent transport, pressure-strain, pressure diffusion and viscous diffusion.

Budgets for the turbulence energy and all Reynolds stresses are shown in figures 20–24 at four streamwise locations within the recirculation region: $x/H = 1.5$, 2, 3 and 4, the first two stations being close to the region where the turbulence-energy production reaches a maximum in the separated shear layer. Data at other locations, including upstream of separation and downstream of reattachment, are available, but are not included herein. All contributions have been normalised by using the scales $U_{\rm in}$ and H. In the following, a number of preliminary comments are made ahead of the discussion of physical interactions implied by the budgets.
First, attention is drawn to the fact that the dissipation rate included in the budgets was obtained so as to balance the sum of the other terms, all associated with large-scale processes. Tests have shown that the resolved dissipation, extracted explicitly from the simulation, is of order of 50–70% of the balance, thus indicating a good resolution even beyond the wave-number separating inertial and highly dissipative ranges.
Second, as noted above, the pressure-velocity interaction is split into (non-deviatoric) pressure-diffusion and (deviatoric) pressure-strain contributions. The latter set of terms in the normal-stress equations are readily shown to formally contract to zero (for incompressible flow), and the validity of this constraint in the present simulations has also been verified explicitly by summing up the normal-stress contributions. The above split of the pressure-velocity interaction is a standard practice, that is held to be useful for second-moment-closure modelling. It is not unique, however, and various rational options for splitting the pressure-velocity term are discussed by Groth [37] and Dejoan et al. [38]. As will be argued in the discussion below, the split does not necessarily aid transparency of the physical interactions. In particular, very close to the wall, the two contributions tend to diverge dramatically, in the case of the streamwise and cross-flow normal stresses (there is no pressure diffusion in the spanwise normal stress), the sum of the two being much smaller than the fragments themselves.
Third, when the cross-flow variation of the various budget contributions for the streamwise stations included, $x/H = 1.5$, 2, 3 and 4, are examined, it is helpful to take note of the thickness of the reverse-flow layer at these streamwise stations, namely: $y_{\rm w}/H = 0.05$, 0.13, 0.3 and 0.05, respectively (see figure 9). The locus of the zero-velocity positions and the zero-streamfunction line, the latter defining the recirculation bubble, is shown in figure 11 (also reported in figure 17).
A final preliminary point to note is the remaining weak unevenness of the curves beyond $x/H = 3.0$, despite a very long time integration period—1700 time units. This reflects the increasing difficulty of obtaining full numerical convergence in the budget contributions, a limitation associated with the increasing predominance of large-scale motions in the separated shear layer. Moreover, beyond separation, the budget contributions decline significantly in magnitude with increasing streamwise distance, so that relative errors, from whatever source, tend to be magnified, especially in the case of the $\overline{vv}$ budgets in which contributions tend to be lowest.

The turbulence-energy budgets (figure 20) confirm one statement made earlier, namely that the separated shear layer is very far away from a state of equilibrium, and this is so especially in the early stages of separation. Thus, at $x/H = 1.5$, the ratio of production to dissipation in the shear layer reaches a value close to 2.5 (the maximum factor is around 3.3, at $x/H = 1.0$—figure 16), while this ratio drops no lower than 2 further downstream. This high level of imbalance reflects the very strong generation of streamwise fluctuations, consistent with the trend

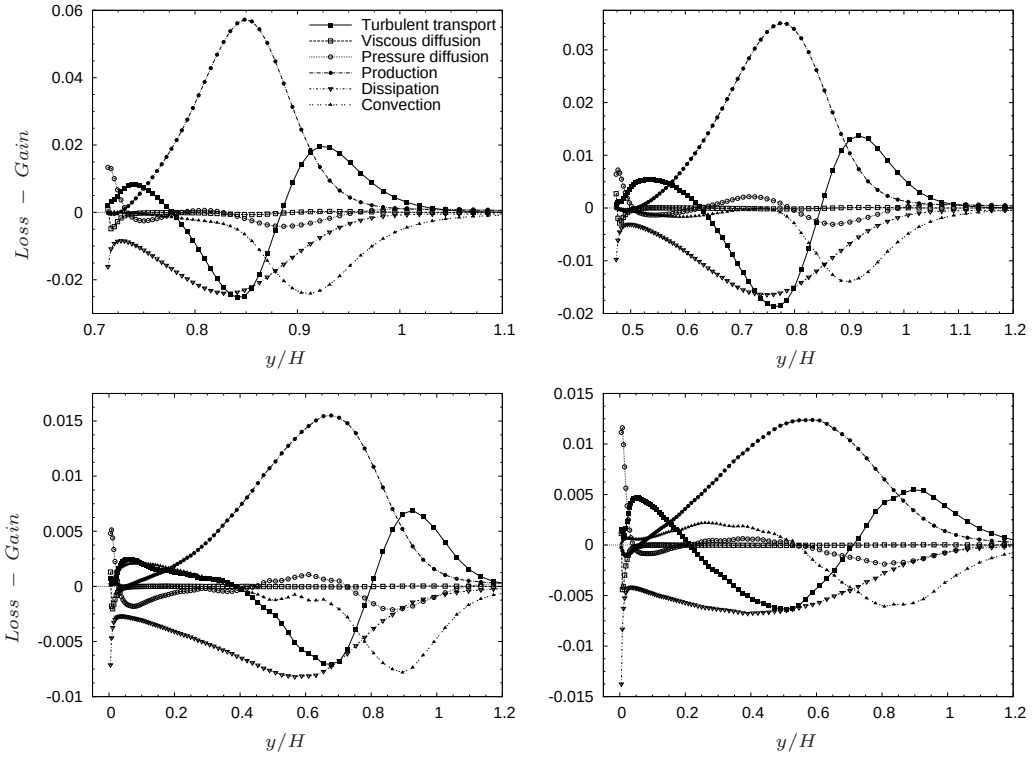

Figure 20. Budgets for k at $x/H = 1.5$, 2 (top), 3 and 4 (bottom).

towards one-component turbulence, as discussed in the previous section. Another important observation—in part a corollary of the previous comment—is that turbulent diffusion is a major contributor to the balance. Indeed, this has to be so in order to compensate for the imbalance between production and dissipation, in the highest-shear portion of the shear layer within which both are close to their respective peaks. Thus, diffusion drains energy from this region and transports it both into the outer part of the shear layer and towards the wall. In the outer part, where both production and dissipation weaken, this diffusion is counteracted mainly by forward convective transport of energy (a loss) in the streamwise direction. Within the reverse-flow layer, but away from the immediate vicinity of the wall, the balance is mainly between turbulent diffusion (gain) and dissipation (loss); shear is low, and this is a region in which the flow shows a trend towards isotropy (see plateau in figure 19(b) at $x/H = 1.5$). Very close to the wall, dissipation is balanced by pressure diffusion (which is identical to the pressure-velocity interaction) and viscous diffusion, the former being a minor contributor elsewhere. This behaviour is in contrast to the near-wall state in attached flow, where the high value of dissipation is balanced by viscous diffusion only, as confirmed also by budgets from the present simulation upstream of separation—e.g. at $x/H = -4$, shown in figure 4(c). The scenario described above is essentially valid throughout the flow region examined, including at the sections $x/H = 3$ and 4, except that the contributions decline as reattachment is approached, because of the progressive decrease in straining.

The budgets for $\overline{uu}$ (figure 21) are similar to those for k in several respects, and this is expected, as the streamwise stress is by far the most important contributor to the energy. However, there are also some significant differences. First and foremost, the pressure-strain process, which is zero in the case of the k-budget, is a very important drain of $\overline{uu}$ over most of the flow, acting together with dissipation and turbulent diffusion, the latter in the centre of the separated shear layer, to

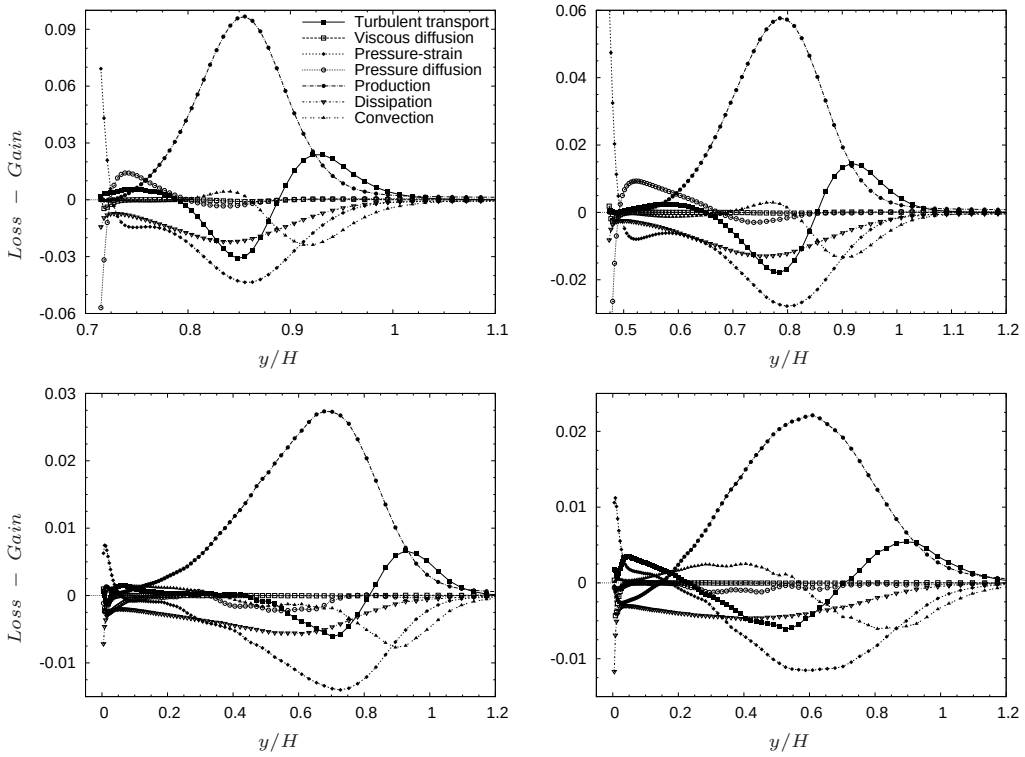

Figure 21. Budgets for $\overline{uu}$ at $x/H = 1.5$, 2 (top), 3 and 4 (bottom).

counteract a production level that exceeds dissipation by a factor of up to 5.5. This term transfers energy to the other two normal stresses—preferentially to $\overline{ww}$, as will transpire later. The low level of the dissipation rate is remarkable, and may be interpreted as indicating that down-scale transfer in the cascade in the shear layer cannot keep pace with the very high rate of production, associated with high levels of shear stress, which then requires turbulent diffusion and pressure-strain redistribution to act as the principal sinks, at least in the heighest-sheared portion of the separated shear layer. A peculiar feature of the pressure-velocity interaction process is the highly localised divergence of the pressure-strain and the pressure-diffusion fragments very close to the wall in the early stages of separation. While the budgets of $\overline{vv}$ will be considered separately below, it is noted here that this divergence is mirrored in that budget through a steep decline in the pressure-strain term and a sharp rise in the pressure-diffusion term. This behaviour is presumed to be linked to the need to secure the asymptotic approach of turbulence to the two-component limit through a rapid decay of wall-normal fluctuations, in the face of the zero-divergence constraint that has to be satisfied by the pressure-strain process. Very close to the wall, this process drains energy from $\overline{vv}$, transferring it to $\overline{ww}$ and $\overline{uu}$. However, this drain, if operating on its own, would drive $\overline{vv}$ into non-realisable negative levels, and this dictates the presence of a counteracting pressure-diffusion process. Analogously, $\overline{uu}$ would be driven to non-realisable, high levels were it not for the counteracting pressure-diffusion term, at least in the early stages of separation. The result of the combination of the two fragments is then a positive pressure-velocity contribution in $\overline{uu}$ (of the same order as the dissipation), a nearly zero contribution in $\overline{vv}$ and a decisively positive contribution (purely a pressure-strain interaction) in $\overline{ww}$—a budget discussed below—which reflects the *splatting* effect at the wall.

Although $\overline{vv}$ is a minor contributor to the turbulence energy, especially close to the wall, its behaviour is extremely important, nevertheless, for it is responsible, in conjunction with the shear strain, for the generation of the shear stress. In

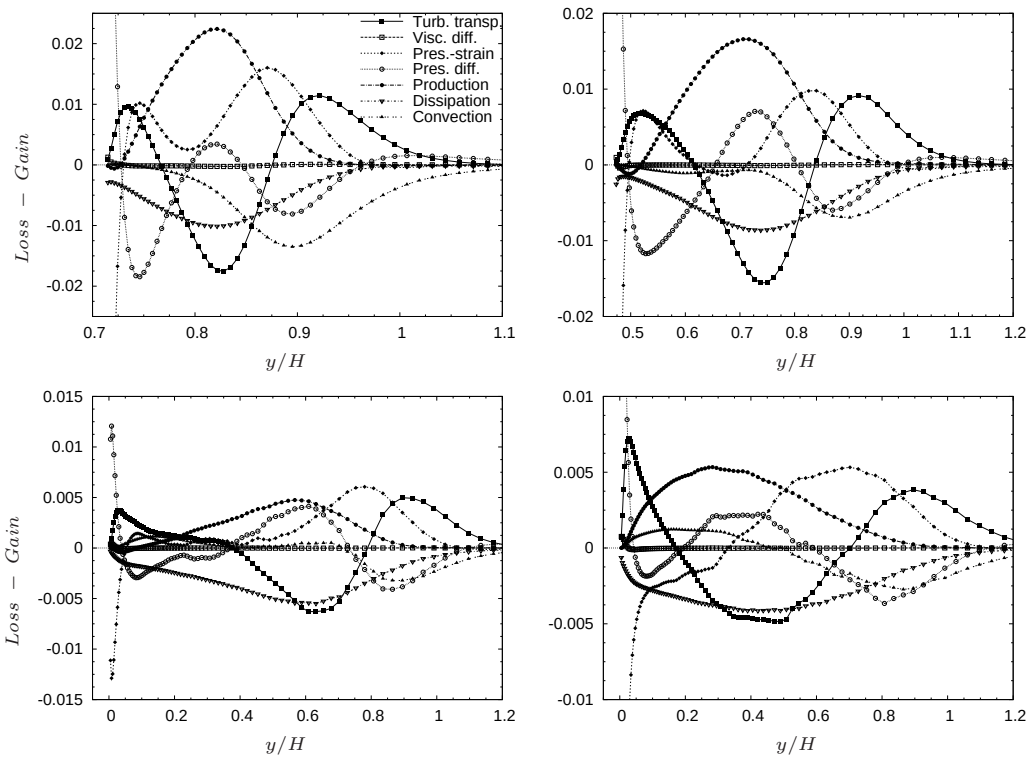

Figure 22. Budgets for $\overline{vv}$ at $x/H = 1.5$, 2 (top), 3 and 4 (bottom).

contrast to the conditions in an attached boundary layer, production of $\overline{vv}$ is, here, a significant contributor to the budget. This production in the highly-sheared portion of the separated layer, in combination with a positive pressure-strain transfer of energy from $\overline{uu}$ to $\overline{vv}$, is counteracted mainly by dissipation and turbulent diffusion, with convection being increasingly important in the outer part of the shear layer. In contrast to the budget of $\overline{uu}$ that for $\overline{vv}$ features a substantial pressure-diffusion contribution outside the immediate near-wall region. Within the reverse-flow layer, this term counteracts the gain in $\overline{vv}$ by the pressure-strain process (except very close to the reattachment point, where the pressure-strain term is itself negative), as turbulence begins to be driven towards the two-component state. In the outer part of the shear layer, the pressure-diffusion term counteracts the gain arising from a strong outward diffusion of $\overline{vv}$ and the high level of the pressure-strain process in the face of a relatively low dissipation rate.

As noted already, the $\overline{ww}$ budget lacks a pressure-diffusion contribution, because of spanwise homogeneity. Moreover, production is zero, for the same raison. With the near-wall region left aside, this budget is largely characterised by a balance between a positive pressure-strain contribution and dissipation, with turbulent diffusion transferring energy from the high-shear central portion of the shear layer to both inner and outer regions, thus aiding dissipation in balancing the gain by the pressure-strain process. As is the case with the other normal stresses, negative convection provides an additional drain in the outer part of the shear layer to compensate for the positive pressure-strain and turbulent-diffusion contributions. An important observation, made earlier when discussing the budget of $\overline{uu}$, but deserving to be highlighted again, is that pressure-strain rises close to the wall. This rise is especially pronounced as the reattachment region is approached, a process that is compensated by increased dissipation, turbulent diffusion and viscous diffusion. This rise in the pressure-strain, associated with splatting, generates large spanwise fluctuations, leading to near-wall normal stress $\overline{ww}$ being of the same order as $\overline{uu}$ (true only near the reattachment), despite the absence of production.

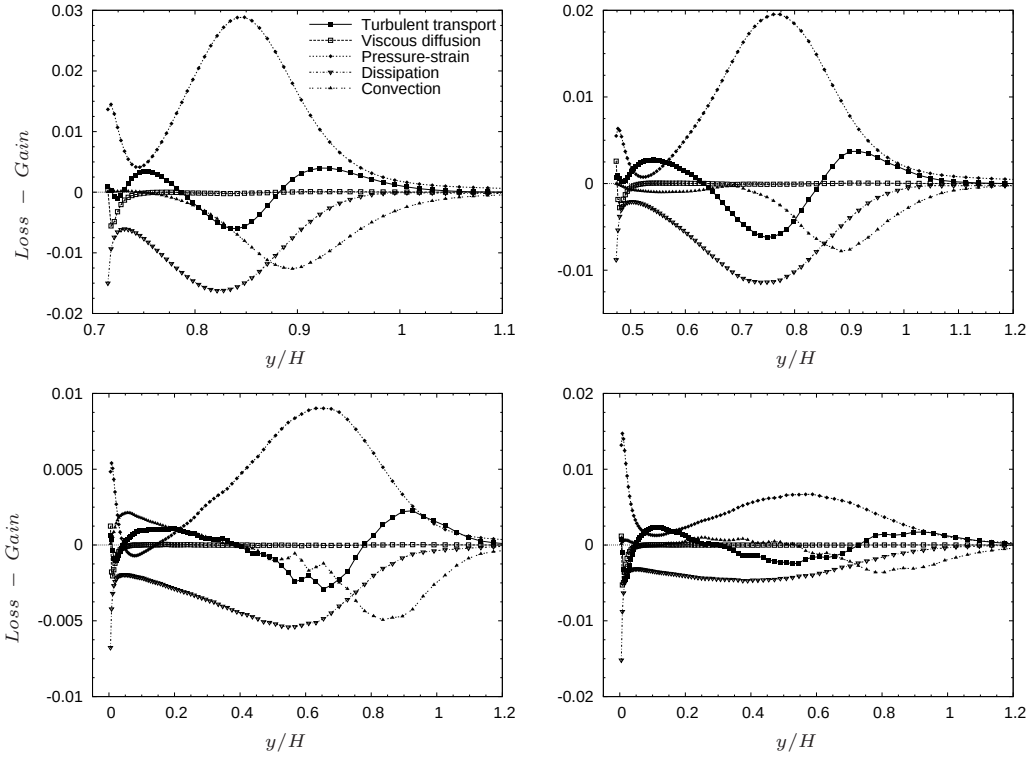

Figure 23. Budgets for $\overline{ww}$ at $x/H = 1.5$, 2 (top), 3 and 4 (bottom).

The shear-stress budget (figure 24) is dominated by negative production—especially large in the initial portion of the separated shear layer—and positive pressure-strain contribution, the latter enhanced by positive turbulent diffusion in the central portion of the shear layer. As expected, dissipation is minor, in the separated shear layer, but also near the wall—the latter less expected, because anisotropy in the small scales is likely to be significant close to the wall. In the former, this reflects the near-isotropy of the dissipative scales, while in the latter region, dissipation is essentially forced to keep pace with the decline in all other terms, especially production and the pressure-strain term, as the shear stress diminished rapidly towards the wall. Pressure diffusion is a relatively minor contributor in the separated shear layer, but more influential in the reverse-flow layer and very close to the wall. In fact, in the reverse-flow layer, pressure diffusion plays the dominant role—much more so than the pressure-strain term—in diminishing the shear stress. Turbulent diffusion, while not negligible in the reverse-flow layer, is not a dominant contributor to the balance. It opposes production in the highly-sheared region and transports shear stress towards the wall and the outer region shear-layer, thus elevating its magnitude in these regions. Very close to the wall, the dramatic reversal and divergence of the two fragments of the pressure-velocity-interaction is observed, and this mirrors the process observed in the $\overline{vv}$ budget.

4.4. *Length scales*

The length scale used most frequently in fully-turbulent flow is the "macro scale", usually expressed as $L = k^{3/2}/\varepsilon$. This scale is held to represent the energetic eddies which are associated with mixing (*i.e.* shear stress, fluxes). It is also the primary length scale that underpins statistical closures, and is regarded as an identifier of the degree of *locality* of turbulence, when compared to the length scale associated with mean-flow straining $L_s = S/|\nabla S|$, where $S = \sqrt{2S_{ij}S_{ij}}$ and S_{ij} is the mean

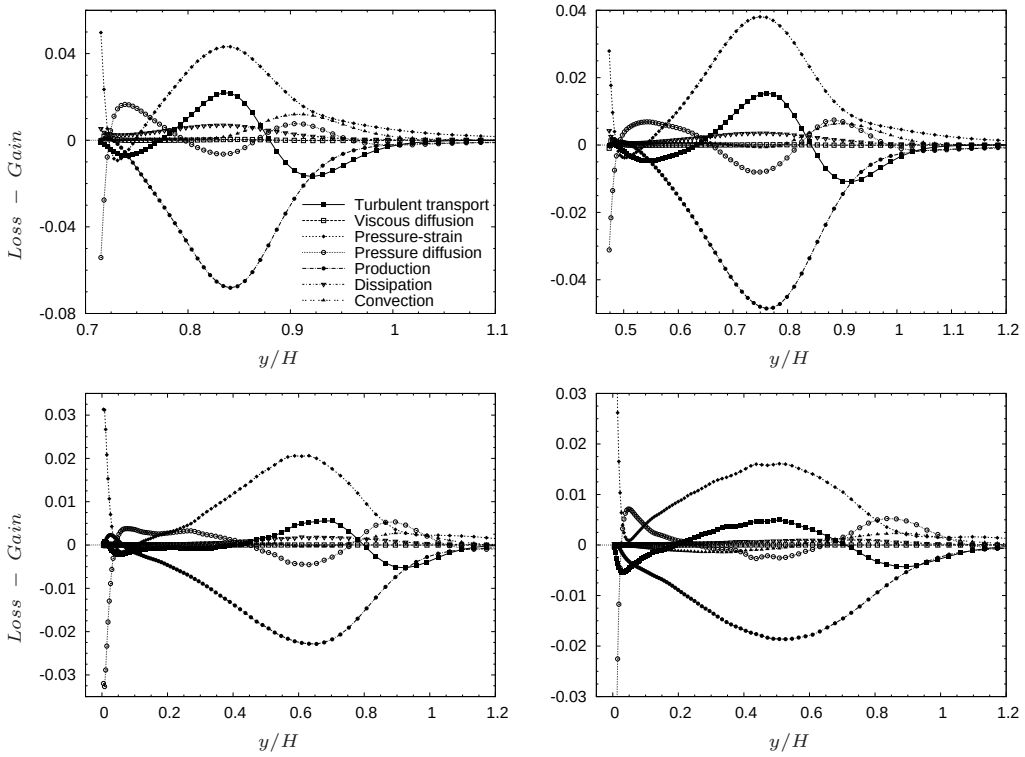

Figure 24. Budgets for $\overline{uv}$ at $x/H = 1.5$, 2 (top), 3 and 4 (bottom).

rate-of-strain tensor. If the former is small, relative to the latter, turbulence can be said to be "localised"; otherwise turbulence is held to be non-local and its state ought to be describable adequately by local analysis (see [39]).

To explore the above issues, the turbulence and mean-flow length scales are shown in figures 25(a) and 25(b), respectively. Both are normalised by the step height H. The macro-scale is relatively low near the wall, especially upstream of separation, scaling with the wall distance broadly within the range y^3 to y, depending on the distance from the wall. It begins to grow rapidly following separation, to reach values 0.5–1.2H within the recirculation zone and in the wake region. The rather uneven map of the length scale in the region beyond $x/H = 3$, especially above $y/H = 0.7$, reflects the influence of two factors. First, and most important, the dissipation values decline rapidly beyond the shear layer, so that slight variations in its value will have a major impact of the length scale, which is indirectly proportional to the dissipation. Second, at around $x/H = 3$, there is a rapid change in the curvature of the grid lines due to a corresponding change in the orientation of the lower wall, and this is aggravated by a coarsening of the normal grid beyond $x/H = 3$ station in the central region, due to the channel expansion (figure 1). However, the overall message is clear, namely that the macro scale is substantial in the recirculation zone, of the order of the height of the separated region.

Both the macro and mean-flow scales are difficult to determine accurately, because they involve the dissipation rate in the former, as noted already, and the derivatives of the strain in the latter. However, figure 25(b) shows the mean-flow scale to be comparable or lower than the macro scale over most parts of the separation zone, and this is brought out in figure 25(c) which shows the ratio of the two scales. Within the recirculation zone, the macro-scale exceeds the mean-flow scale by a factor of 1.5–4, with levels above 10 arising in the reverse-flow layer. These

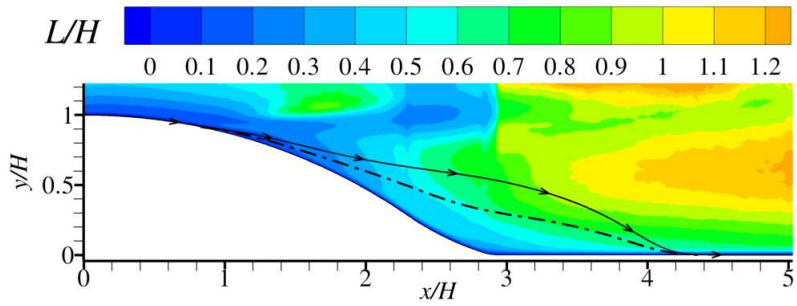

(a) Turbulence (or macro) lengthscale.

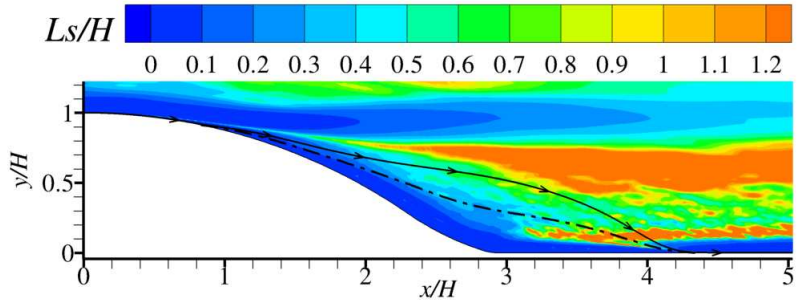

(b) Mean-flow lengthscale.

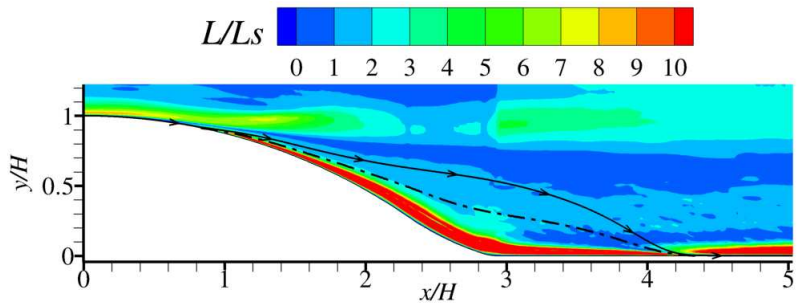

(c) Ratio of the above scales.

Figure 25. Contours of turbulence length-scale $L = k^{3/2}/\varepsilon$, mean-flow length scale $L_s = S/|\nabla S|$ (both normalized by H), and their ratio L/L_s.

results lead to the supposition that single-point closure, of whatever ilk, is likely to highly challenged when used to model this flow.

5. Conclusions

The present study was motivated by the wish, and the need, to gain insight into the complex processes occurring when a boundary layer undergoes separation along a gently curving wall, and develops a shallow and relatively weak recirculation zone, in which—as it turns out—the flow is never unconditionally reversed at any point in the recirculation zone. Despite the weakness of the separation, with the mean reverse-flow velocity not exceeding 13% of the free-stream value, the overall influence of the separation on the flow is significant. In particular, separation is accompanied by a substantial modification of the pressure distribution, especially at the wall, and by a strong elevation in the turbulence activity, relative to the conditions in an attached boundary layer.

Important time-mean characteristics of the flow include: an extremely tenuous

separation process, with very shallow separation angle, a thin reverse-flow layer that hugs the wall, and is thus strongly affected by it, a reattachment at a very shallow angle and a pronounced wall-pressure plateau within the recirculation zone.

The separation process was shown to occur over a significant proportion of the surface, giving rise to a region of intermittently attached and separated boundary layer. This intermittency extends over virtually the entire surface, post separation, and within the recirculation zone, one manifestation being a high level of skin-friction variance. In the mean, the boundary layer initially experiences acceleration upstream of the curved step, followed by deceleration and destabilizing inflexion as it approaches separation.

One consequence of the unsteady separation is an especially high growth rate in the turbulence level in the initial stretch of the separated shear layer. In statistical terms, this is due to turbulence generation exceeding dissipation by a factor rising above 3. Much of this imbalance is due to the very strong generation of streamwise fluctuations, which give rise to a layer that has some characteristics akin to that of one-component turbulence. Throughout the separated shear layer, this high level of production-to-dissipation ratio renders the state of this layer far from turbulence-energy equilibrium. Anisotropy in the shear layer is high, with the minimum value of the flatness parameter, A, progressing from around 0.05 immediately after separation to around 0.4, at the position of maximum normalized Reynolds shear stress, $-\overline{uv}/k$, to around 0.6 in the post-reattachment wake.

The strong departure of the flow from a state of turbulence equilibrium, throughout the flow, is also given expression by substantial levels of turbulent diffusion and—especially in the outer portion of the separated layer—also convection of the second moments. Typically, turbulent diffusion plays the influential role of draining energy from the centre of the shear layer and redistributing it towards the wall and out into the outer reaches of the shear layer. The variation of the pressure-velocity interaction terms is complex. A dominant, expected, feature of the pressure-strain process is a transfer of energy from the streamwise stress to the other two normal-stress components, *i.e.* a process enhancing isotropisation. However, this process is generally opposed by the pressure diffusion fragment. This is so especially very close to the wall, where the two fragments virtually neutralise each other, and in the case of the cross-flow normal stress $\overline{vv}$ in which pressure diffusion is as important as pressure-strain and plays a crucial role in driving turbulence towards the two-component wall limit. These observations lead to the conclusion that the split of the pressure-velocity interaction into pressure-strain and pressure-diffusion contributions is not advantageous in terms of the insight it offers.

Finally, it is expected that the results of this study will contribute to validation and testing of computational schemes for general separated flows, incorporating models, either for the whole spectrum of turbulence or portions thereof.

Acknowledgement

The contribution of the lead author to the research documented in this paper was supported by the EC project ATAAC, 7$^{\text{th}}$ Framework Programme (No. ACP8–GA–2009-233710-ATAAC).

References

[1] R.L. Simpson, *Turbulent boundary-layer separation*, Annual review of fluid mechanics 21 (1989), pp. 205–232.

[2] H. Le, P. Moin, and J. Kim, *Direct numerical simulation of turbulent flow over a backward-facing step*, Journal of Fluid Mechanics 330 (1997), pp. 349–374.
[3] H.T. Huang, and H.E. Fiedler, *A DPIV study of a starting flow downstream of a backward-facing step*, Experiments in Fluids 23 (1997), pp. 395–404.
[4] A.F. Heenan, and J.F. Morrison, *Passive control of backstep flow*, Experimental Thermal and Fluid Science 16 (1998), pp. 122–132.
[5] T. Lee, and D. Mateescu, *Experimental and numerical investigation of 2-D backward-facing step flow*, Journal of Fluids and Structures 12 (1998), pp. 703–716.
[6] P.G. Spazzini, G. Iuso, M. Onorato, N. Zurlo, and G.M. Di Cicca, *Unsteady behavior of back-facing step flow*, Experiments in Fluids 30 (2001), pp. 551–561.
[7] J. Tihon, J. Legrand, and P. Legentilhomme, *Near-wall investigation of backward-facing step flows*, Experiments in Fluids 31 (2001), pp. 484–493.
[8] I. Lee, and H.J. Sung, *Characteristics of wall pressure fluctuations in separated and reattaching flows over a backward-facing step: Part I. Time-mean statistics and cross-spectral analyses*, Experiments in Fluids 30 (2001), pp. 262–272.
[9] H.J. Kaltenbach, *Turbulent flow over a swept backward-facing step*, European Journal of Mechanics - B/Fluids 23 (2004), pp. 501–518.
[10] J. Fröhlich, C. Mellen, W. Rodi, L. Temmerman, and M. Leschziner, *Highly resolved large-eddy simulation of separated flow in a channel with streamwise periodic constrictions*, Journal of Fluid Mechanics 526 (2005), pp. 19–66.
[11] M. Breuer, N. Peller, C. Rapp, and M. Manhart, *Flow over periodic hills-numerical and experimental study in a wide range of Reynolds numbers*, Computers & Fluids 38 (2009), pp. 433–457.
[12] K. Abe, Y.J. Jang, and M.A. Leschziner, *An investigation of wall-anisotropy expressions and length-scale equations for non-linear eddy-viscosity models*, International Journal of Heat and Fluid Flow 24 (2004), pp. 181–198.
[13] C. Wang, Y.J. Jang, and M.A. Leschziner, *Modelling two- and three-dimensional separation from curved surfaces with anisotropy-resolving turbulence closures*, International Journal of Heat and Fluid Flow 25 (2004), pp. 499–512.
[14] S. Jakirlić, R. Manceau, S. Šarić, A. Fadai-Ghotbi, B. Kniesner, S. Carpy, G. Kadavelil, C. Friess, C. Tropea, and J. Borée, *LES, Zonal and Seamless Hybrid LES/RANS: Rationale and Application to Free and Wall-Bounded Flows Involving Separation and Swirl*, Numerical Simulation of Turbulent Flows and Noise Generation (2009), pp. 253–282.
[15] J. Neumann, and H. Wengle, *Coherent structures in controlled separated flow over sharp-edged and rounded steps*, Journal of Turbulence 5 (2004), pp. 1–24.
[16] B. Wasistho, and K. Squires, *Prediction of turbulent separation over a backward-facing smooth ramp*, Journal of Turbulence 6 (2005), pp. 1–26.
[17] S. Radhakrishnan, U. Piomelli, A. Keating, and A.S. Lopes, *Reynolds-averaged and large-eddy simulations of turbulent non-equilibrium flows*, Journal of Turbulence 7 (2006), pp. 1–30.
[18] J. Dandois, E. Garnier, and P. Sagaut, *Numerical simulation of active separation control by a synthetic jet*, Journal of Fluid Mechanics 574 (2007), pp. 25–58.
[19] W.A. El-Askary, *Turbulent boundary layer structure of flow over a smooth-curved ramp*, Computers & Fluids 38 (2009), pp. 1718–1730.
[20] M. Garcia-Villalba, N. Li, W. Rodi, and M.A. Leschziner, *Large-eddy simulation of separated flow over a three-dimensional axisymmetric hill*, Journal of Fluid Mechanics 627 (2009), pp. 55–96.
[21] D. You, M. Wang, and P. Moin, *Large-Eddy simulation of flow over a wall-mounted hump with separation control*, AIAA Journal 44 (2006), pp. 2571–2577.
[22] S. Šarić, S. Jakirlić, A. Djugum, and C. Tropea, *Computational analysis of locally forced flow over a wall-mounted hump at high-Re number*, International Journal of Heat and Fluid Flow 27 (2006), pp. 707–720.
[23] A. Avdis, S. Lardeau, and M.A. Leschziner, *Large Eddy Simulation of Separated Flow over a Two-dimensional Hump with and without Control by Means of a Synthetic Slot-jet*, Flow, Turbulence and Combustion 83 (2009), pp. 343–370.
[24] D. Greenblatt, K.B. Paschal, C.S. Yao, J. Harris, N.W. Schaeffler, and A.E. Washburn, *Experimental investigation of separation control. Part 1: Baseline and steady suction*, AIAA Journal 44 (2006), pp. 2820–2830.
[25] S. Song, and J.K. Eaton, *Reynolds number effects on a turbulent boundary layer with separation, reattachment, and recovery*, Experiments in Fluids 36 (2004), pp. 246–258.
[26] S. Radhakrishnan, U. Piomelli, and A. Keating, *Wall-modeled large-eddy simulations of flows with curvature and mild separation*, Journal of Fluids Engineering 130 (2008), p. 101203.
[27] M. Marquillie, J.P. Laval, and R. Dolganov, *Direct numerical simulation of a separated channel flow with a smooth profile*, Journal of Turbulence 9 (2008), pp. 1–23.
[28] S. Lardeau, and M.A. Leschziner, *The interaction of round synthetic jets with a turbulent boundary layer separating from a rounded ramp*, to appear in Journal of Fluid Mechanics (2011).
[29] S. Zhang, and S. Zhong, *An experimental investigation of turbulent flow separation control by an array of synthetic jets*, AIAA Paper 2010-4582 (2010).
[30] G.M. Fishpool, and M.A. Leschziner, *Stability bounds for explicit fractional-step schemes for the Navier-Stokes equations at high Reynolds number*, Computers & Fluids 38 (2009), pp. 1289–1298.
[31] C.M. Rhie, and W.L. Chow, *Numerical study of the turbulent flow past an aerofoil with trailing edge separation*, AIAA Journal 21 (1983), pp. 1525–1532.
[32] M. Manhart, N. Peller, and C. Brun, *Near-wall scaling for turbulent boundary layers with adverse pressure gradient*, Theor. Comput. Fluid Dyn. 22 (2008), pp. 243–260.
[33] T.S. Lund, X. Wu, and K.D. Squires, *Generation of Turbulent Inflow Data for Spatially-Developing Boundary Layer Simulations* 1*, Journal of Computational Physics 140 (1998), pp. 233–258.
[34] J. Jiménez, S. Hoyas, M.P. Simens, and Y. Mizuno, *Turbulent boundary layers and channels at moderate Reynolds numbers*, Journal of Fluid Mechanics (2010), pp. 1–26.

[35] M. Inagaki, T. Kondoh, and Y. Nagano, *A Mixed-Time-Scale SGS Model With Fixed Model-Parameters for Practical LES*, Journal of Fluids Engineering 127 (2005), p. 1.

[36] H.T. Kim, S.J. Kline, and W.C. Reynolds, *The production of turbulence near a smooth wall in a turbulent boundary layer*, Journal of Fluid Mechanics 50 (1971), pp. 133–160.

[37] J. Groth, *Description of the pressure effect in the Reynolds stress transport equationd*, Physics of Fluids 3 (1991), pp. 2276–2277.

[38] A. Dejoan, C. Wang, and M.A. Leschziner, *Assessment of Turbulence Models for Predicting the Interaction Region in a Wall Jet by Reference to LES Solution and Budgets*, Flow, Turbulence and Combustion 77 (2006), pp. 229–255.

[39] J.C.R. Hunt, and A.M. Savill, *Guidelines and criteria for the use of turbulence models in complex flows*, In: Hewitt, G.F., Vassilicos, J.C. (eds.) Prediction of Turbulent Flows (2005), pp. 291–343.